frontiers in Marine Science

ORIGINAL RESEARCH
published: 15 July 2020
doi: 10.3389/fmars.2020.00568

Processes Driving Iron and Manganese Dispersal From the TAG Hydrothermal Plume (Mid-Atlantic Ridge): Results From a GEOTRACES Process Study

David González-Santana[1], Hélène Planquette[1], Marie Cheize[1,2], Hannah Whitby[1†], Arthur Gourain[3], Thomas Holmes[4†], Vivien Guyader[2], Cécile Cathalot[2], Ewan Pelleter[2], Yves Fouquet[2] and Géraldine Sarthou[1]*

[1] CNRS, IRD, Ifremer, LEMAR, University of Brest, Plouzané, France, [2] Ifremer, Géosciences Marine, LCG, Plouzané, France, [3] Department of Ocean Sciences, School of Environmental Sciences, University of Liverpool, Liverpool, United Kingdom, [4] The Institute for Marine and Antarctic Studies, University of Tasmania, Hobart, TAS, Australia

Hydrothermal vents are a recognized source of trace elements to the ocean inventory. Nevertheless, the contribution of slow-spreading ridges remains poorly resolved. To address this, high-resolution dissolved (<0.45 μm) iron (dFe) and manganese (dMn) samples were collected during the GEOTRACES HERMINE GApr07 process study at the Mid Atlantic Ridge. Samples were collected at nine stations, from the TAG vent site to 75 km south-southwest following the neutrally buoyant plume. Concentrations of dMn and dFe ranged from 71 ± 6 and 51 ± 2 nmol kg^{-1} right above the vent site to 0.43 ± 0.01 and 1.56 ± 0.02 nmol kg^{-1} at the most distal station, respectively. Using a 5-box model coupled with our data, we show that as the plume traveled away from the vent, aggregation processes controlled dFe concentrations in the first 2 km, with an aggregation rate averaging between 8.0 ± 0.6 and 0.11 ± 0.04 nmol L^{-1} d^{-1}, respectively in the first and second kilometer. Aggregation, likely of small colloidal particles, led to partitioning of the size fractionated Fe pool, as 6% of the dFe was moved into the particulate size fraction. Further away, disaggregation processes became more prevalent, with rates ranging from 0.27 ± 0.02 to 0.008 ± 0.001 nmol L^{-1} d^{-1}, enriching the dFe pool by 10%. The computed decrease of hydrothermal Fe within the neutrally buoyant plume was likely caused by flocculation of small Fe oxyhydroxide particles. This process resulted in Fe aggregate formation with radii estimated to range between 14 and 20 μm in the first km from TAG. Between 2 and 30 km from the vent site, the radii ranged between 2 and 4 μm.

Keywords: iron, manganese, hydrothermal, TAG, Mid Atlantic Ridge, GEOTRACES

OPEN ACCESS

Edited by:
Johan Schijf, University of Maryland Center for Environmental Science (UMCES), United States

Reviewed by:
William M. Landing, Florida State University, United States
Torben Stichel, Alfred Wegener Institute Helmholtz Centre for Polar and Marine Research (AWI), Germany
Robert Sherrell, Rutgers, The State University of New Jersey, United States

****Correspondence:***
David González-Santana
david.gonzalezsantana@univ-brest.fr

†Present address:
Hannah Whitby, Department of Ocean Sciences, School of Environmental Sciences, University of Liverpool, Liverpool, United Kingdom
Thomas Holmes, School of Oceanography, University of Washington, Seattle, WA, United States

Specialty section:
This article was submitted to Marine Biogeochemistry, a section of the journal Frontiers in Marine Science

Received: *21 January 2020*
Accepted: *22 June 2020*
Published: *15 July 2020*

Citation:
González-Santana D, Planquette H, Cheize M, Whitby H, Gourain A, Holmes T, Guyader V, Cathalot C, Pelleter E, Fouquet Y and Sarthou G (2020) Processes Driving Iron and Manganese Dispersal From the TAG Hydrothermal Plume (Mid-Atlantic Ridge): Results From a GEOTRACES Process Study. Front. Mar. Sci. 7:568. doi: 10.3389/fmars.2020.00568

INTRODUCTION

The Trans-Atlantic Geotraverse (TAG) active mound is situated on the Mid Atlantic Ridge (MAR) (26° 8′ N, 44° 50′ W) at a depth of around 3620 m and corresponds to a seafloor massive sulfide mound measuring 250 m in diameter and 50 m in height. TAG active mound was the first high-temperature hydrothermal vent found at a slow-spreading oceanic ridge during the NOAA

Trans-Atlantic Geotraverse project in 1985 (Rona et al., 1986). Since then, TAG has become one of the most comprehensively studied seafloor hydrothermal fields and is well characterized in terms of activity (e.g., Lalou et al., 1995), fluid composition (e.g., Von Damm, 1995), and deposits (e.g., Mills et al., 2001).

Since the widespread interest in oceanic iron (Fe) started in the late 1980s (Martin and Fitzwater, 1988), multiple "new" Fe sources (Boyd and Ellwood, 2010) have been investigated, including atmospheric dust, resuspension of coastal and shallow sediments, ice melting, vertical diffusive flux, volcanism, bottom pressure torque, and hydrothermal activity (e.g., Tagliabue et al., 2017). Recently, the observed basin-scale impact of the East Pacific Rise hydrothermal site has revived interest in hydrothermal sites, pointing them out as a far-field source of some trace elements and isotopes (TEIs) (Resing et al., 2015; German et al., 2016; Fitzsimmons et al., 2017). Nevertheless, to date, the contribution of slow-spreading ridges to the trace metal pools is poorly constrained (German et al., 2016). The persistence of the hydrothermal anomaly in the water column is affected by physical and chemical speciation processes, including complexation with organic ligands and the formation of iron-sulfide colloidal nanoparticles (Luther et al., 1992; Fitzsimmons et al., 2017). This last process is even more favorable at TAG than in other close-by hydrothermal sites at the MAR, due to its high-sulfide content (Rona, 2005).

In the absence of important external sources, the vertical distribution of dissolved iron (dFe) in the ocean presents a nutrient-like profile, indicative of its biological role, with near constancy at depths below 1000 m ($\sim$0.7 nmol L^{-1}, Johnson et al., 1997; Boyd and Ellwood, 2010). In contrast, dissolved manganese (dMn) concentrations in deep waters, in the absence of submarine manganese sources such as hydrothermal activity and sediment inputs, are low and uniform (Statham et al., 1998), ranging from 0.1 to 0.2 nmol kg^{-1} in the Central Atlantic Ocean (Hatta et al., 2015). Since 1985, the combination of positive anomalies of dMn and increases in suspended matter have been used as a tracer for hydrothermal plumes including the TAG neutrally buoyant plume (Klinkhammer et al., 1986; Speer and Marshall, 1995).

Hydrothermal vents act as potentially major sources of trace metals (TMs) to the deep Atlantic Ocean (e.g., Tagliabue et al., 2010). Previously, models have tried to represent the relative role played by ridges in different ocean basins. However, they have encountered significant uncertainties caused by the scarcity of data from slow-spreading ridges (German et al., 2016; Tagliabue and Resing, 2016) especially at distances further than 1 km from high-temperature vent sites. This was previously described during the 1990s when German and Sparks (1993) emphasized the need to study the TAG hydrothermal plume over scales of 1–10 km, based on the re-entrainment results from their particle recycling model, where sinking particles can get reintroduced into the plume, potentially desorbing Fe. The combination of TAG's location and its hydrothermal venting results in an input of numerous chemical components into the relatively newly formed North Atlantic Deep Water with an important dispersion potential due to the global thermohaline conveyor (Statham et al., 2005).

Recent studies have indicated that hydrothermal plumes present a nearly conservative dFe behavior (Resing et al., 2015), with plumes extending from short distances in the Atlantic, Indian, Arctic, and Southern oceans (Middag et al., 2009, 2011; Nishioka et al., 2013; Saito et al., 2013; Conway and John, 2014; Measures et al., 2015) to far-field in the Pacific (Resing et al., 2015; Fitzsimmons et al., 2017). Both Fe-stabilizing ligands (Bennett et al., 2008; Sander and Koschinsky, 2011) and unreactive Fe nanoparticles or colloids (Yücel et al., 2011) should regulate the stabilization of Fe against loss from solution. High- and low-temperature vents have different discharged metal concentrations, hydrogen sulfide concentrations and high biological activity, together with degradation of biomass, specific synthesis by microbial activities and abiotic formation of organic molecules that could be potential sources of dissolved organic molecules in both types of vents (Sander and Koschinsky, 2011). Ligands also form organically complexed Fe(II) species present during buoyant plume rise, potentially lowering the Fe(II) oxidation rate (Bennett et al., 2008). Stimulated by observations of Fe distributions in the near-field neutrally buoyant plume at 9°45′N on the Northern East Pacific Rise, Field and Sherrell (2000) calculated Fe(II) oxidation rates for a variety of vent sites in the Atlantic and Pacific as a function of ambient deepwater pH, oxygen, temperature, salinity and pressure, based on inorganic kinetic rate constant data of Millero et al. (1987), and concluded that half-lives for Fe(II) oxidation and the resultant formation of Fe oxyhydroxide particles should vary substantially among vent sites in different ocean basins, from 20 min to >6 h. The only field study to test this prediction was carried out at Indian Ocean vent sites, and the rate observations largely supported these predictions, while suggesting the possibility that Fe(II) interactions with dissolved organic matter may slightly modify the governing equations (Statham et al., 2005).

In this context, one of the primary goals of the HERMINE process study cruise (GEOTRACES GApr07; doi: 10.17600/17000200) was to understand the dispersal and biogeochemical reactivity of Fe and Mn within the TAG hydrothermal plume, along the mixing continuum with seawater. Here, we present the concentrations of dFe and dMn measured at 9 stations in close vicinity to TAG in order to describe their variability inside the neutrally buoyant plume (NBP). This unprecedented high sampling resolution provides an in-depth view of the reversible exchanges occurring within the NBP. The model presented in this paper takes into account most of the state-of-the-art processes controlling Fe behavior along hydrothermal plumes in the oceans and could be applied to characterize its distribution in slow spreading ridges.

MATERIALS AND METHODS

Seawater samples were collected during the HERMINE GApr07 process study cruise around the TAG hydrothermal site (**Figure 1**). The cruise took place during spring 2017 (13th March to 28th April) onboard the French Research Vessel N/O *Pourquoi Pas?*

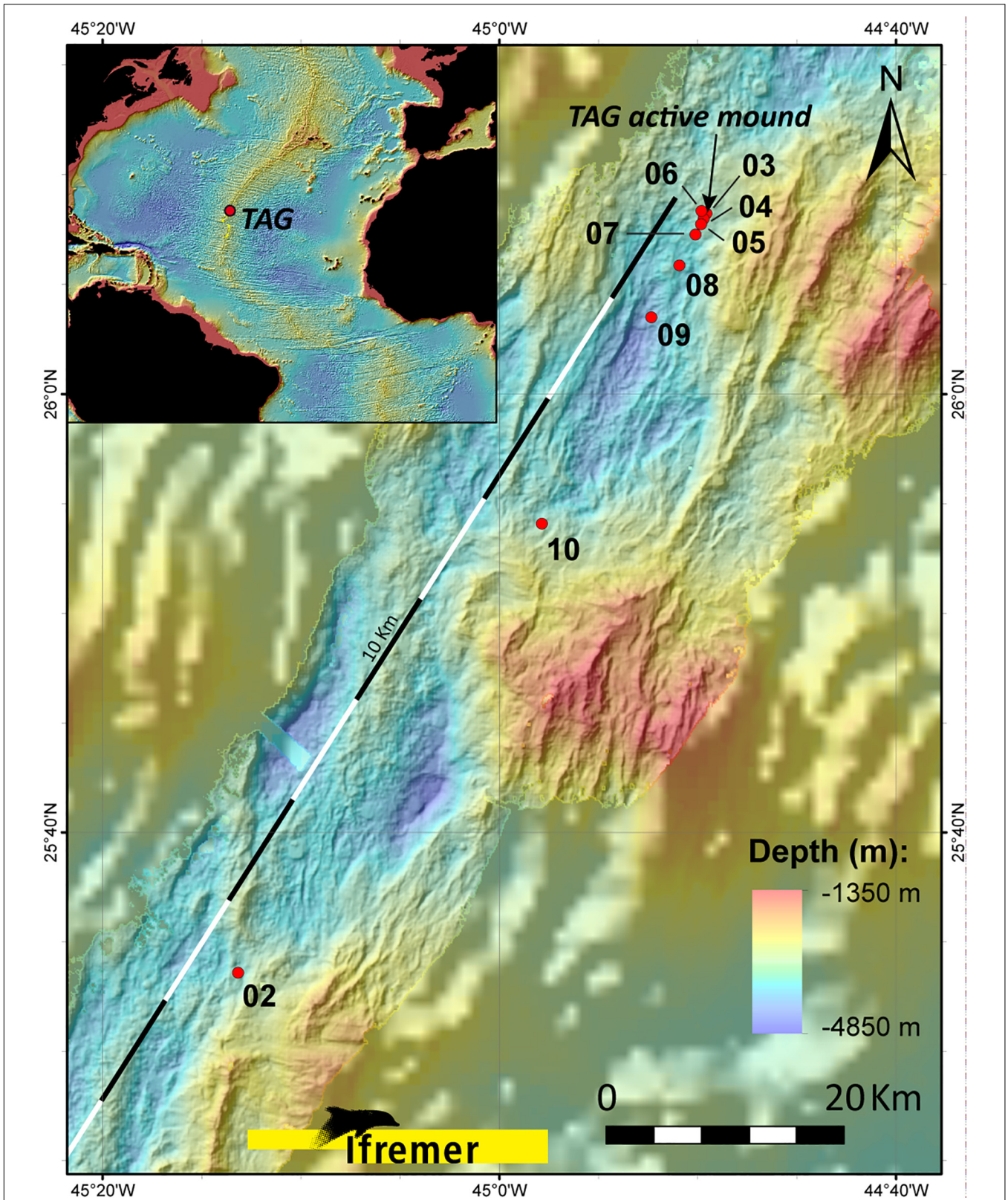

FIGURE 1 | Bathymetric map of the Mid-Atlantic Ridge around the TAG hydrothermal mound. Red circles represent stations where the trace metal rosette was deployed. Station 3 was deployed at the mound, station 6 was deployed 0.5 km to the west. Stations 4, 5, 7, 8, 9, 10 and 2 were respectively deployed 0.5, 1, 2, 5, 10, 30, and 75 km SSW of TAG. Inset is an index map of the location of the TAG hydrothermal site in the North Atlantic Ocean.

Sampling Strategy

The sampling strategy allowed for high-resolution sampling within the TAG rising and distal NBP. Onboard Lowered Acoustic Doppler Current Profiler (L-ADCP) combined with the TM-clean rosette fitted with a conductivity temperature depth sensor (CTD, Seabird 911plus) and suspended matter data were processed in real time so that the NBP could be followed while maintaining the highest possible spatial resolution. The highest suspended matter values (0.089 NTU) were measured at the NBP depths at station 6, located 0.5 km west (W) from the vent site (26° 8.4′ N, 44° 49.8′ W). However, TAG is situated in the rift valley of the MAR. As a result, while the plume is initially transported westward the ridge blocks its pathway and thus the plume does not follow a straight, uninterrupted path (**Figure 1**). This is especially prevalent at depths deeper than 3000 m.

After deploying a L-ADCP at TAG, a clear 229° angle was observed in the current direction at the depth of maximum suspended matter signal (Mastin, 2020). In light of these results, it was thus decided to follow the south-southwest (SSW) direction, with NBP suspended matter values reaching 0.086 NTU 0.5 km from the vent site. Stations were therefore arranged along the current flow path, with increasing distance SSW from the vent site, at 0.5, 1, 2, 5, 10, 30, and 75 km (**Figure 1**). For this study, sampling efforts concentrated on the NBP, with half of the sampling depths encompassed inside the NBP (between 2965 and 3607 m), and almost two-thirds of the chosen depths being deeper than 2500 m.

Sample Collection and Analysis

Seawater samples were collected according to the GEOTRACES guidelines[1], using a TM-clean polyurethane powder-coated aluminum frame rosette equipped with twenty-four 12-L, externally closing, Teflon-lined, GO-FLO bottles (General Oceanics) and attached to a Kevlar® line. The cleaning protocols for sampling bottles and equipment also followed the GEOTRACES Cookbook.

Upon recovery of the TM rosette, GO-FLO bottles were transported to a class ISO 6 TM-clean sampling van equipped with an ISO 5 laminar flow hood. The bottles were inverted three times to avoid settling of particles and pressurized to <50 kPa with 0.2 μm filtered dinitrogen (N_2, Air Liquide). Sub-samples for dissolved TMs were collected in TM-clean low-density polyethylene bottles (Nalgene®) after filtration through acid-cleaned 0.45 μm pore-size polyethersulfone filters (Supor®, 25 mm) mounted on Swinnex® filter holders, following Planquette and Sherrell (2012). Seawater samples were then acidified to ∼ pH 1.7 using hydrochloric acid (HCl, Ultrapure® Merck) under an ISO 5 laminar flow hood, double bagged, and stored at ambient temperature in the dark before shore-based analysis.

Trace metal measurements were carried out within 12 months after collection on a SF-HR-ICP-MS Element XR instrument (Thermo Fisher, Bremen, Germany), at Pôle Spectrométrie Océan (IFREMER, France). The spectrometer was coupled to an ESI seaFAST-pico® introduction system and run with a method analytically similar to that of Lagerström et al. (2013). Calibrations were performed using low trace metal concentration internal seawater with known standard additions of a mixed solution containing Fe, Mn, Cu, Co, Ni, Pb, and Zn. Nine-point calibrations were performed at the beginning, half-way and at the end of the run. The average slope of the first and second calibrations was used for the first half of the samples, while the second and third calibration were used for the second half of the samples. This standard addition technique effectively minimized the sensitivity differences caused by the matrix effect. We performed an internal standardization using 10 ppb In (indium) in order to correct the changes of sensitivity of our instrument. Four triplicate reference materials (SAFe S, SAFe D2, GSC, and GSP, **Table 1**) were analyzed daily during each analytical run to ascertain accuracy and precision. Analyzed SAFe standards were validated with the consensus values, but we could not validate for the GSC and GSP standards. Precision was further assessed through duplicate samples (every 10th sample was a duplicate). The computed average dMn and dFe deviation from duplicate measurements of the same sample with concentrations < 1.5 nmol kg^{-1} was 64 and 66 pmol kg^{-1}, respectively (n = 44). The standard deviation of the reported concentrations was calculated from the duplicate analysis of samples combined with the concentration determination from the three daily calibration curves. The detection limit (defined as three times the standard deviation of the blank) was 0.018 nmol L^{-1} for both elements.

[1]http://www.geotraces.org/images/Cookbook.pdf

RESULTS

Gauging Hydrothermal Imprint Using Physical Properties

Physical properties such as potential temperature (θ), salinity (S), potential density (σ), and suspended matter were closely monitored to identify the hydrothermal signal (θ and σ have been computed using ocean surface as the reference value). At the vent site station, at depths greater than 3145 m, variations in the physical properties of seawater were associated with hydrothermal activity (**Figure 2A**). The hydrothermal source produced a plume, the buoyant plume (BP), that was less dense than the surrounding water. The BP ascended until its density reached the density of the surrounding water, thereby transforming into the NBP. A θ-S plot (**Figure 3A**) shows three main differences with respect to a profile of a non-hydrothermally affected station. The hydrothermal imprint on the water column was still clearly visible 0.5 and 1 km SSW of TAG (**Figures 3B,C**), with increases in θ-S at both stations. At these distances, the NBP was better mixed, as interpreted from the lack of crossover of deeper waters in the θ-S plot (**Figure 3A** inside the ellipse compared to **Figures 3B–D**). The hydrothermal θ-S signal was lost 2 km SSW of TAG (**Figure 3D**).

Higher than background levels of suspended matter observed hundreds of meters above the sea floor indicated the presence of increased concentrations of suspended particulate matter, which are characteristic of hydrothermal plumes (German et al., 1996). At the vent site, two suspended matter maxima were observed.

TABLE 1 | Intercomparison reference material values obtained during the analysis of the samples.

CRM		SAFE D2			SAFE S			GSP			GSC		
		Average	*SD*	*n*	Average	*SD*	*n*	Average	*SD*	*n*	Average	*SD*	*n*
dMn (nmol kg^{-1})	This study	0.34	0.07	20	0.76	0.07	9	0.18	0.08	4	0.61	0.08	18
	Consensus	0.35	0.05		0.79	0.06		0.78	0.03	9	2.18	0.08	8
dFe (nmol kg^{-1})	This study	0.96	0.08	20	0.16	0.01	9	0.26	0.01	4	1.09	0.11	18
	Consensus	0.93	0.02		0.09	0.01		0.16	0.05	11	1.54	0.12	13

Shown are the average concentrations in nmol kg^{-1}, standard deviation in nmol kg^{-1} and the number of replicates.

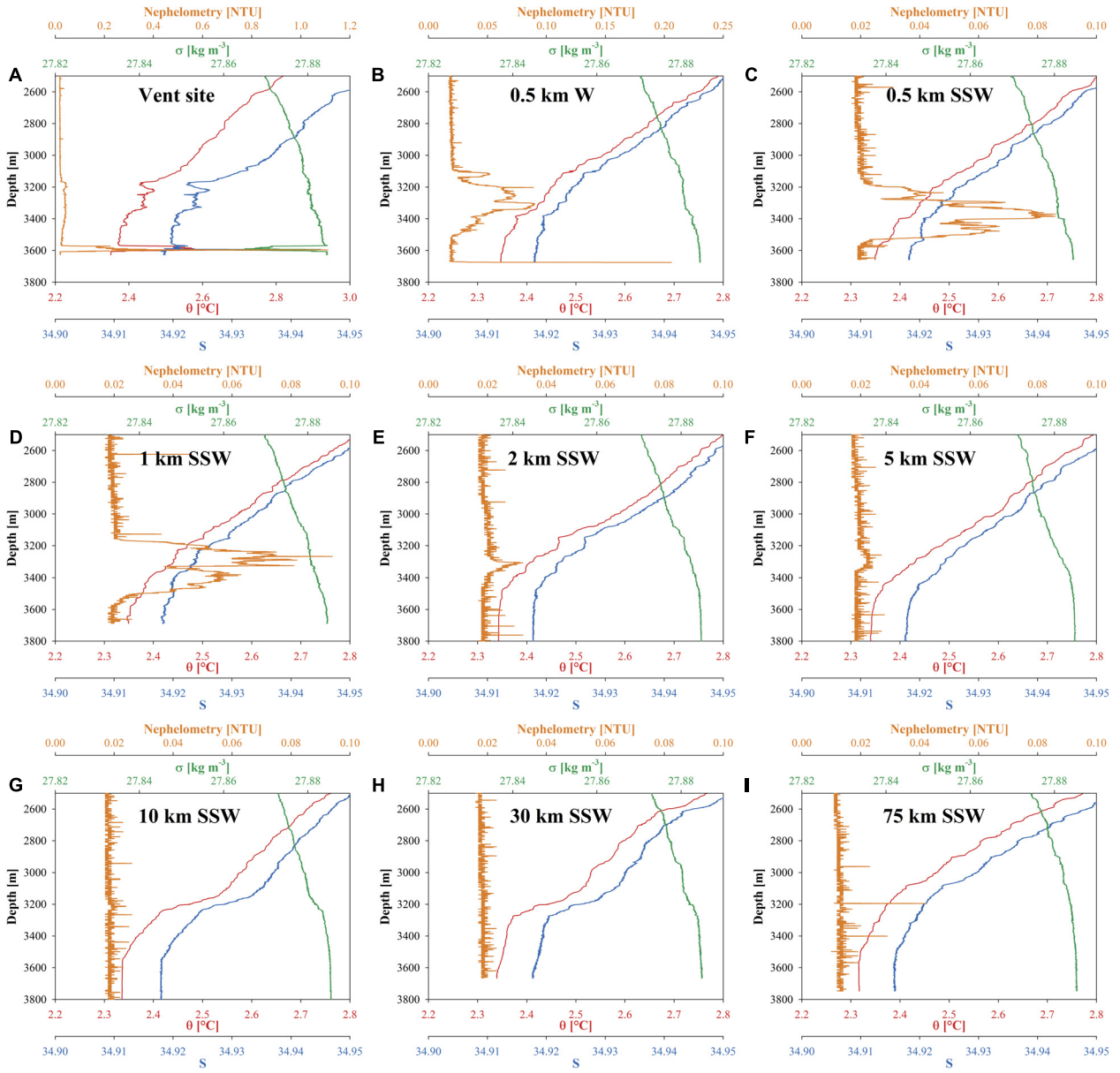

FIGURE 2 | Vertical profiles for depths deeper than 2500 m of potential temperature θ (red), salinity *S* (blue), potential density σ (green), and suspended matter/nephelometry (orange) for station situated at TAG vent site (**A**; Stn 3), 0.5 km W (**B**; Stn 6), 0.5 km SSW (**C**; Stn 4), 1 km SSW (**D**; Stn 5), 2 km SSW (**E**; Stn 7), 5 km SSW (**F**; Stn 8), 10 km SSW (**G**; Stn 9), 30 km SSW (**H**; Stn 10) and 75 km SSW of TAG (**I**; Stn 2).

A deep maximum next to the vent site between 3563 and 3607 m (1.11 NTU) and a shallower maximum between 3167 and 3475 m (0.05 NTU) corresponding to the NBP signal (**Figure 2A**). The maximum suspended matter signal, observed close to the sediment bed, does not result solely from hydrothermal activity, but instead reflects a combination of hydrothermal particles and resuspended sediments. Following the SSW direction, pronounced increases with respect to background levels in suspended matter were observed in the first 10 km from the TAG site (**Figures 2A–G**). At 30 km SSW, the suspended matter signal was reduced by 98% with respect to the maximum observed at the vent sites' BP which made it impossible to clearly differentiate the depth at which the NBP was located.

Previous studies have reported TAG's NBP to ascend 300–400 m above the seafloor (Klinkhammer et al., 1986; Rona and Speer, 1989; German et al., 1991a), with the core of the plume detected at depths of 3200–3500 m (German et al., 1991b; Goto et al., 2007; Hatta et al., 2015). In this study, the maximum suspended matter signal in the NBP ranged from 3385 m deep at 0.5 km SSW of TAG (**Figure 2B**) to 3210 m at 10 km SSW (**Figure 2G**), remaining within the previously reported depth ranges, but ascending 175 m in the first 10 km. We attribute the ascension of the plume to water mass transport. The high suspended matter signal at the NBP was bordered by water masses of two densities, of σ = 27.880 kg m^{-3} and σ = 27.883 kg m^{-3} above and below, respectively. At the vent site, the BP was situated between 3455 and 3555 m, while the NBP was found between 3165 and 3455 m. The NBP could be located using the changes in the gradients of θ, *S*, and σ (σ = 27.880 and 27.883 kg m^{-3}, **Figures 2H,I**). This confirmed that its upper limit continuously shallowed from 3165 to 3110 m and its thickness decreased from 442 m at the vent site (Stn 3), to 138 m 5 km from the vent site (Stn 8), followed by an increase up to 205 m 10 km from the vent site (Stn 9). The variable thickness can be caused by internal waves generated from having two water masses, the plume and the surrounding water, which have different densities and could move at different speeds, as can be observed at the Rainbow hydrothermal site (van Haren et al., 2017).

Suspended matter results also showed the existence of a deep nepheloid layer, below 3800 m, from 2 km SSW of TAG and extending through until 10 km SSW of TAG (**Figure 4A**). This left a vertical "buffer" zone greater than 400 m between the NBP and the benthic nepheloid layer, preventing any direct interactions between the pools of particles. Dissolved Fe and dMn concentrations in the buffer zone were significantly lower than in the bottom section of the NBP (see **Figures 4A,B**), further confirming there was no interference from the nepheloid layer on the NBP.

Hydrothermal Imprint on Trace Metal Distribution

The vertical and horizontal distribution of TMs can help us to understand Fe and Mn residence times in the water column and their transport across ocean basins. Past work at the fast-spreading East Pacific Rise revealed a hydrothermal plume which transported dFe over 4000 km (Resing et al., 2015; Fitzsimmons et al., 2017). Similarly, in the South Atlantic Ocean, slow-spreading ridges have been suggested to export dFe over 1000 km, reaching the Southern Ocean (Saito et al., 2013). Although geological conditions differ between these sites, previous existing datasets at TAG describe a hydrothermal plume with a potential impact between 20 and 1000 km away from its source (Rona, 1980; Klinkhammer et al., 1986; Conway and John, 2014).

The mixing of hydrothermal fluid with seawater results in the production of particulate matter. In the NBP, the most common precipitates are collectively referred to as oxyhydroxides, which are characteristic components of marine sediments in hydrothermal zones (Nelsen et al., 1987). Due to their chemical composition, these hydrothermally produced particles act as efficient scavengers for many trace elements from the surrounding seawater (Pichler and Veizer, 1999).

In 2010–2011, the U.S. GEOTRACES North Atlantic Cruises: GEOTRACES GA03w (Hatta et al., 2015) crossed the North Atlantic Ocean, zonally crossing the TAG hydrothermal vent during the transect. Stations unaffected by coastal and shelf margins or hydrothermal emissions showed an average background dFe and dMn concentrations for the deep ocean (>2500 m) from 0.6 to 0.8 nmol kg^{-1} and from 0.1 to 0.2 nmol kg^{-1}, respectively.

In contrast, the concentrations of both of these metals within the TAG hydrothermal fluids can be orders of magnitude higher, with end member concentrations of 5.1 $\pm$ 0.5 mM and 0.69 $\pm$ 0.02 mM respectively for Fe and Mn (Chiba et al., 2001). Within the NBP, dFe, and dMn concentrations of up to 68 and 33 nM were measured during the GA03w cruise (Hatta et al., 2015). According to previous work (Edmonds et al., 1996; Chiba et al., 2001), the black smoker fluid composition has not shown any significant changes over time.

Dissolved Manganese Distributions

At the vent site station, the dMn maximum was found at 3605 m depth (approximately 45 m above the seafloor), reaching 71.2 $\pm$ 5.6 nmol kg^{-1} (**Figure 5A**). This high dMn concentration could be due to hydrothermal activity and/or caused by sediment interactions, such as resuspension, diffusion, tidal pumping of porewaters and bioirrigation (Elderfield, 1977; Noble et al., 2012; Cheize et al., 2019), although there was no increase in pMn. At 3580 m depth, dMn concentrations decreased to 0.14 $\pm$ 0.01 nmol kg^{-1}, which is in the upper range of dMn background level concentrations (0.10–0.15 nM, Hatta et al., 2015; van Hulten et al., 2017). Ascending from 3555 m to 3204 m, dMn concentrations in the BP and the NBP increased to a local maximum of 35.6 $\pm$ 2.8 nmol kg^{-1}. From 3204 m to 3104 m concentrations decreased to background levels.

Half a kilometer west of TAG (**Figure 5B**), three variations within the plume were observed with maximum dMn concentrations located between 3100 and 3410 m (**Figure 5B**). Similarly, 0.5 km SSW of TAG (**Figure 5C**), three plume variations were observed, although the two shallowest variations were located 50 m deeper than their counterparts to the west (**Figure 5C**). At the station situated 1 km SSW (**Figure 5D**), the lower plume variation remained at the same depth (3404 m),

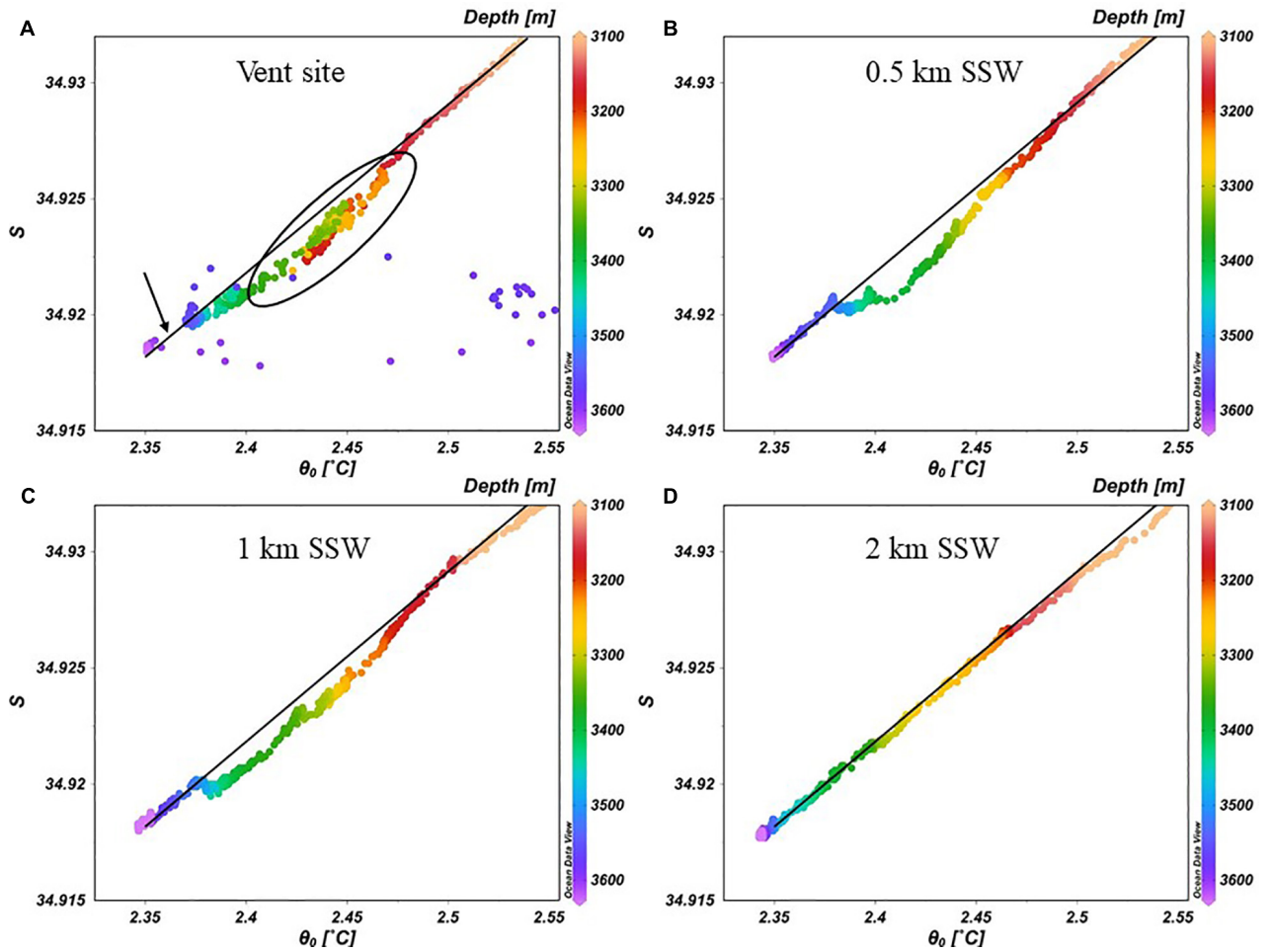

FIGURE 3 | θ-S relation in the water column at the TAG site **(A)**, 0.5 km SSW **(B)**, 1 km SSW **(C),** and 2 km SSW **(D)**. The potential temperatures increased with respect to background levels as a response to the introduction of warm hydrothermal fluid (datapoints diverge from the straight line). The arrow points to a missing section located around 3607 m as a result of sampling close to the hydrothermal vent, which showed 0.5°C warmer (up to 2.85°C) and saltier water than background level values, but in agreement with a hydrothermal source (Rudnicki and Elderfield, 1993; Goto et al., 2007). The hydrothermal source produced a plume, the buoyant plume (BP), that was less dense than the surrounding water. The ascension of the BP caused a non-linearity in θ-S with depth between 3165 and 3370 m. The BP ascended until its density reached the density of the surrounding water, thereby transforming into the NBP (ellipse).

while the upper two plume variations combined and were situated at 3255 m. Further away, at 2 km SSW, there were no variations within the plume (**Figure 5E**), and the dMn maximum was located at 3305 m depth. The dMn profile shape at these stations followed the same trend as nephelometry (**Figure 4A**), adding further evidence that we sampled multiple plume sections.

Dissolved Mn concentrations reached up to 0.43 ± 0.01 nmol kg^{-1} (maximum at 3355 m) 75 km SSW of TAG, more than twice the expected background concentrations (0.10–0.15 nM) (van Hulten et al., 2017). The persistence of dMn 75 km away from the vent site, suggests slow oxidation rates of dMn along the spatial scales considered in our study. Previous work performed at TAG has used dMn as a hydrothermal tracer for the TAG NBP (Klinkhammer et al., 1986; Speer and Marshall, 1995). To evaluate the possibility of using dMn as a hydrothermal tracer, we considered that precipitation processes could affect the distribution of dMn through transfer to the particulate pool. As pMn concentrations remained orders of magnitude lower than dMn through all stations (58 ± 30 pmol kg^{-1}, n = 196; Cheize et al., 2018), and in agreement with the global deep ocean pMn concentration ∼25 pM (van Hulten et al., 2017), it seems that, at the spatial scale of our study, precipitation of dMn is therefore unlikely to be a major loss term of dMn with respect to dilution of the NBP. Accordingly, and in agreement with previous studies (e.g., Field and Sherrell, 2000), we considered dMn as a conservative tracer at the TAG NBP, whose only loss term was dilution and dispersion.

Dissolved Iron Distribution

Overall, dFe profiles exhibited similar behavior to dMn profiles, with some discrepancies between dFe and dMn observed at the vent site station (**Figure 5A**). In contrast to dMn and turbidity maxima, the dFe maximum was not observed at the vent depth (3605 m; 32.1 ± 1.4 nmol kg^{-1}), but was found higher in the

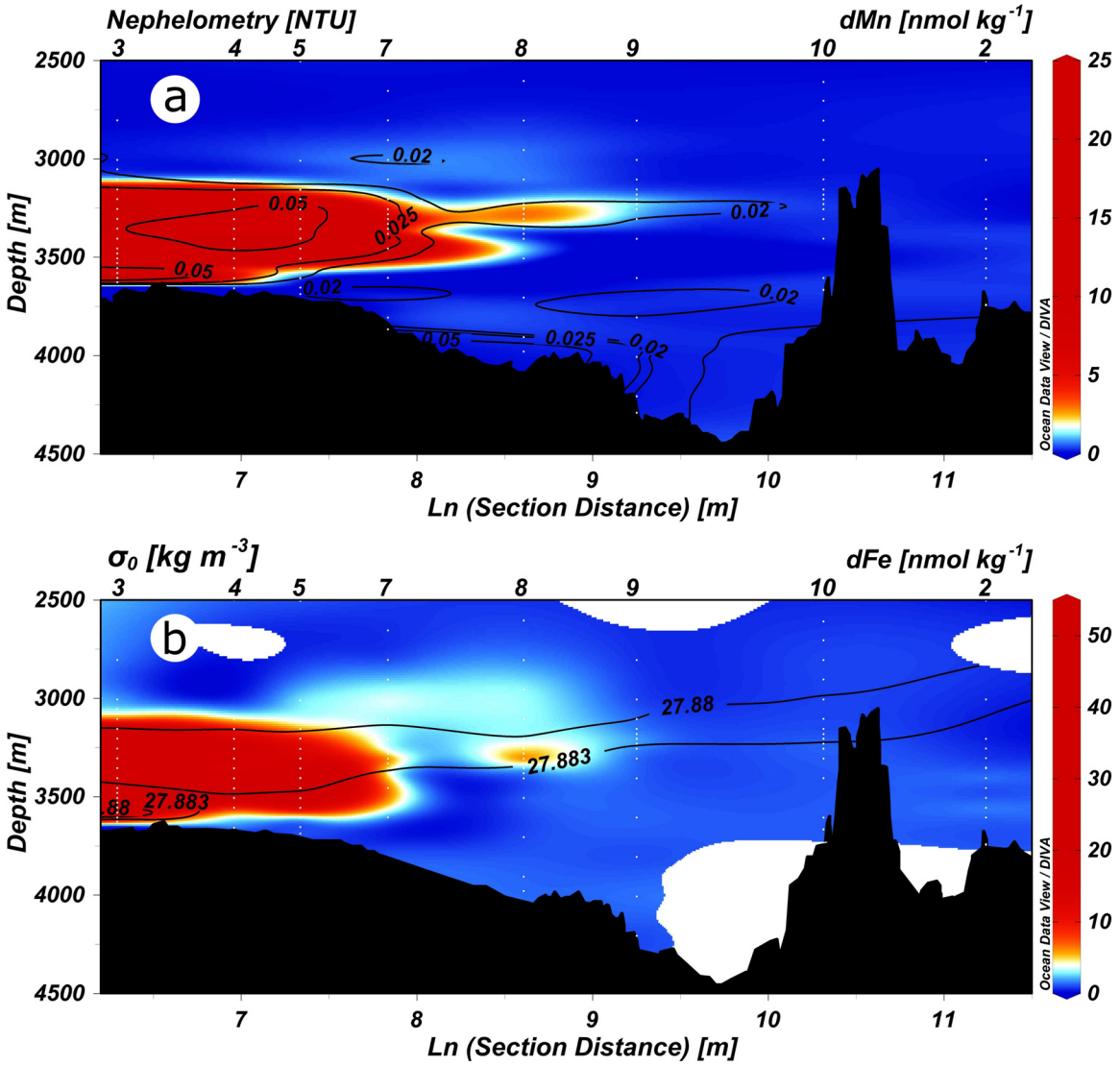

FIGURE 4 | Zonal concentration distribution for dissolved manganese with nephelometry contours **(a)**, and dissolved iron with the 27.880 and 27.883 kg m^{-3} isopycnals **(b)**, following the SSW TAG hydrothermal neutrally buoyant plume. In the bottom *x*-axis, a natural logarithmic scale of the distance in meters is used in order to provide better visual resolution of the station properties. Station numbers are shown on the top *x*-axis. White dots represent depths at which there is a data point for the specific variable.

water column at the top of the NBP. The lack of dFe maximum at the vent depth can be explained by aggregation/adsorption of Fe into the particulate Fe (pFe; grain/mineral or aggregate collected on the 0.45 μm pore size filter), leaving only 8% of the total Fe (TFe = dFe + pFe) in the dissolved phase, compared to 34% at the dFe maximum. Nevertheless, the apparently "low" dFe:dMn ratio could also be explained from manganese enriched sediments (Noble et al., 2012; Cheize et al., 2019). Entrainment of Mn rich sediment porewaters, diffusion into overlying bottom waters and recycling of Mn oxides could create and maintain the elevated dMn that we measured. In parallel, these Mn oxides could also scavenge any surrounding dFe (Machado-Infante et al., 2016).

The vertical dFe profile at the TAG vent station presented more homogeneous concentrations in the BP (3555 m to 3455 m; 33 ± 1 nmol kg^{-1}; n = 5) than in the shallower NBP (3405 m to 3165 m; 31 ± 13 nmol kg^{-1}; n = 5), as observed in the θ and S profiles (**Figure 2A**). Water tank experiments of multi-phase plumes (including gas, different density and size of particles (including the colloidal size) and the soluble phase) in uniform and stratified crossflows have shown that multi-phase plumes behave as mixed single-phase plumes up to a critical height, after which the particulate phase separates from the plume (Socolofsky and Adams, 2002). This would explain the more homogeneous concentrations in the BP and the variability in the NBP. To corroborate this hypothesis,

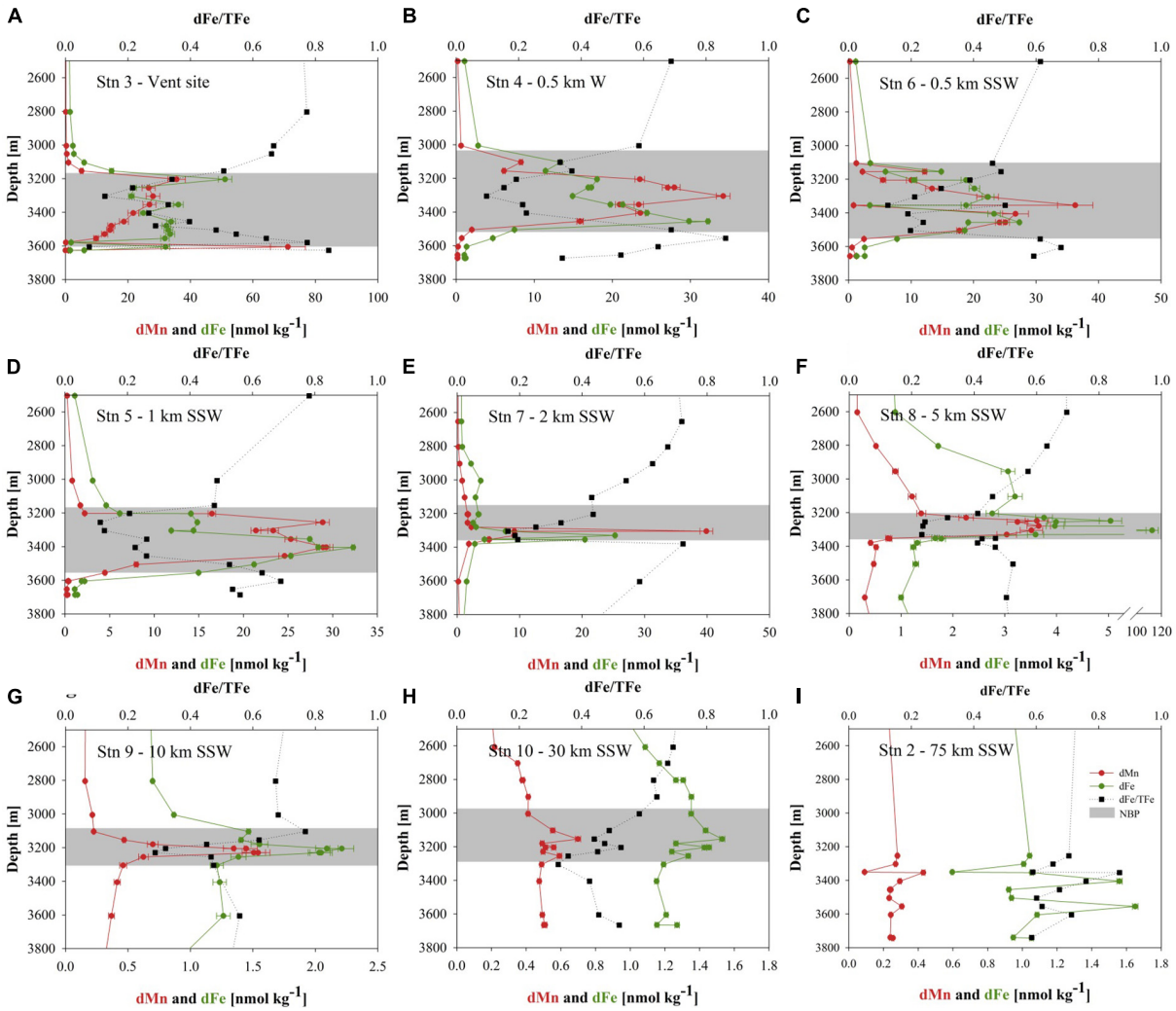

FIGURE 5 | Vertical profiles for dMn (red circles), dFe (green circles), and the fraction of dFe as the total Fe pool (black squares) at stations located at TAG vent site (**A**; Stn 3), 0.5 km W (**B**; Stn 6), 0.5 km S (**C**; Stn 4), 1 km SSW (**D**; Stn 5), 2 km SSW (**E**; Stn 7), 5 km SSW (**F**; Stn 8), 10 km SSW (**G**; Stn 9), 30 km SSW (**H**; Stn 10) and 75 km SSW of TAG (**I**; Stn 2). The gray shading shows the NBP depth using σ = 27.880 and 27.883 kg m^{-3}.

future studies could determine the chemical composition of colloids and particles collected at different depths within the NBP, and combine this information with the physical properties. Dissolved Fe concentrations were still elevated compared to background levels 75 km SSW of TAG (**Figure 5I**) following the NBP dispersion direction. Even though the maximum dFe concentration (1.65 $\pm$ 0.02 nmol kg^{-1}) was less than 2% of the maximum concentration measured at the hydrothermal vent site, the values in the bottom 500 m of the profile (1.11 $\pm$ 0.25 nmol kg^{-1}) were double the reported background level concentration. Analogous studies found transport over greater distances (Saito et al., 2013; Fitzsimmons et al., 2015; Hatta et al., 2015) suggesting the elevated dMn and dFe concentrations detected 75 km from the vent site at depths deeper than 3200 m could be a result of the hydrothermal transport from TAG. Previous research in hydrothermal environments has shown that the dFe would mainly comprise colloidal species, while the dMn would be predominantly soluble (Fitzsimmons et al., 2017), though we could not determine with certainty the origin and pathway of these elevated concentrations due to lack of ancillary hydrothermal tracers.

DISCUSSION

Our results demonstrated that the transport of both dMn and dFe could be observed at least up to 30 km from the vent site. Nevertheless, the discrepancies between dFe and dMn profiles pointed to possible divergences in the transport of these two dTMs. Basin-scale transport of hydrothermally generated TM in fast-spreading ridges has previously been attributed to the reversible exchange dynamics between dissolved and particulate phases that may occur in the NBP (Fitzsimmons et al., 2017). With this in mind, we developed a 5-box model to reveal the

importance of distinctive processes that could affect both TMs differently. Consequently, this model presents the evolution of Fe within the plume and the contribution of each loss term as the NBP was transported away from the vent site.

Model Assumptions

The design of the model follows a simple 5-box model (**Figure 6**). The box height was calculated from the NBP using the σ = 27.880 and 27.883 kg m^{-3} isopycnals. The lengths of the boxes were chosen from the sampled stations situated at the vent site, and at 1, 2, 5, 10, and 30 km away. The third dimension was given to the model by fixing its width to 1 m, to obtain the TM inventory in m^3. With this we eliminated extra assumptions on how the transverse horizontal concentrations of the NBP varied. To better constrain the width of the NBP, transversal tow-yos would have been required.

During the HERMINE cruise, all sampling stations followed the hydrothermal plume and no stations were carried out in non-hydrothermally affected waters. Consequently, water situated above and below the NBP could potentially be affected by the hydrothermal signal. Therefore, to calculate the excess of dMn and dFe in the water column, we subtracted the background level concentrations using the 2010–2011 U.S. GEOTRACES North Atlantic Cruises: GEOTRACES GA03w (Hatta et al., 2015) which took place at the same latitude (crossing the TAG vent field) and assumed background dFe to be 0.70 nmol kg^{-1} and dMn to be 0.15 nmol kg^{-1}. To account for aggregation and disaggregation, all pFe and particulate Mn (pMn) concentrations were obtained from Cheize et al. (2018). Due to the low and stable pMn concentrations through all the samples (58 ± 30 pmol kg^{-1}, n = 196), we assumed that the interactions between the dissolved and particulate pools of Mn are negligible (Field and Sherrell, 2000). Dissolved Mn was used as a conservative tracer, to identify the processes affecting the Fe distribution.

The model considers that the deep ocean is in steady state. Background level concentrations were considered constant throughout the water column. Only one source of TMs was considered to influence the system: the TAG source located at distance 0 km. With respect to the TM data, two assumptions were required. First, that the rosette was deployed crossing the core axis of the NBP. Second, we assumed that linear interpolation between the different data points in a profile faithfully represented the NBP concentrations (straight lines in **Figure 5**).

Finally, based on L-ADCP data (Mastin, 2020), the horizontal velocity was rounded to 1.5 cm s^{-1} throughout the whole model to calculate the horizontal fluxes between boxes. This horizontal velocity agrees with the average value computed by Wichers (2005) from 50 h of results from a deployed ADCP.

Model Design

Modeled stations (MStns) were renamed by their location in the model (vent site, 1, 2, 5, 10, 30 km SSW of TAG as MStn 0–5. This produced five boxes ($1 < |n| < 5$), with sides $h_{|n-1}$ (left side, **Figure 6**) and $h_{|}n$ (right side) calculated from the NBP height; the length ($l_{|n|}$; m) calculated from the distance between the stations, and the width (w = 1 m) was assumed to be constant. Thus, the plume is modeled as a tall narrow wall of varying height with distance from the plume.

Each box had an average concentration ($[I_{|n|}]$; mol m^{-3}; Equation 1), a volume $V_{|n|}$ (Equation 2), and a total inventory ($Q[i_{|n|}]$ mol; Equation 3) of element i,

$$[I_{|n|}] = \frac{1}{h_{|n}} \int_{NBP_{bottom}}^{NBP_{top}} \rho \cdot \left([i_{|nh}] - [i_{bg}]\right) dh_{|n} \quad (1)$$

$$V_{|n|} = \frac{h_{|n-1} + h_{|n}}{2} \cdot l_{|n|} \cdot w \quad (2)$$

$$Q_{i|n|} = [I_{|n|}] \cdot V_{|n|} \quad (3)$$

Where $[I_{|n|}]$ is calculated from the integrated excess inventory (Equation 1) using the measured concentration ($[i_{|nh|}]$; mol m^{-3}) at station n and depth h on the right side of the box, the background concentration ($[i_{bg}]$; mol m^{-3}), the potential density (ρ; kg m^{-3}) and the height of the integrated area ($h_{|n}$; m). The data point at 3305 m at MStn 3 (5 km from TAG) was flagged as an outlier and therefore not considered due to its significantly higher concentration, compared to both the surrounding concentrations and compared to the vent site station.

Four types of fluxes were considered in the model and reported on Equations 4–8 (units and results shown in **Table 2**). For each species i, a horizontal hydrothermal advective flux ($H_{i|n|}$) in the export direction of the plume (positive x-axis, **Figure 6**) was implemented. This flux went both in ($H_{i|n-1}$) and out ($H_{i|n|}$) of each box (Equation 4) and was calculated using the horizontal velocity $\overrightarrow{u}$, the concentration at the left side of the box $[i_{|nh|}]$ and the area of the left side of the box ($h_{|n-1} \cdot w$).

$$H_{i|n|} = [I_{|n|}] \cdot \overrightarrow{u} \cdot h_{|n} \cdot w \quad (4)$$

We considered the existence of two endmembers, the hydrothermally affected seawater from the vent site, and the non-hydrothermally affected seawater. A conservative mixing of both of these two endmembers could be computed using the excess dMn as the tracer found in the hydrothermally affected endmember which would be diluted (i.e., decreasing its concentration by mixing with seawater) and/or dispersed (i.e., physical transport of high concentrated water mass to less concentrated areas) ($Dil_{i|n|}$; Equations 5–6) with the non-hydrothermally affected seawater. Since $Dil_{i|n|}$ represented the conservative mixing of the two endmembers, $Dil_{i|n|}$ of dFe and pFe was proportional to the percentage decrease of dMn (Equation 6).

$$Dil_{dMn|n|} = H_{i|n-1|} - H_{i|n|} \quad (5)$$

$$Dil_{i|n|} = Dil_{dMn|n|} \cdot \frac{Q_{i|n|}}{Q_{dMn|n|}} \quad (6)$$

In the case of Fe, two more fluxes were considered, an aggregation/disaggregation process ($A_{|n|} > 0$ and $A_{|n|} < 0$, respectively) between dFe and pFe pools and the sinking of pFe

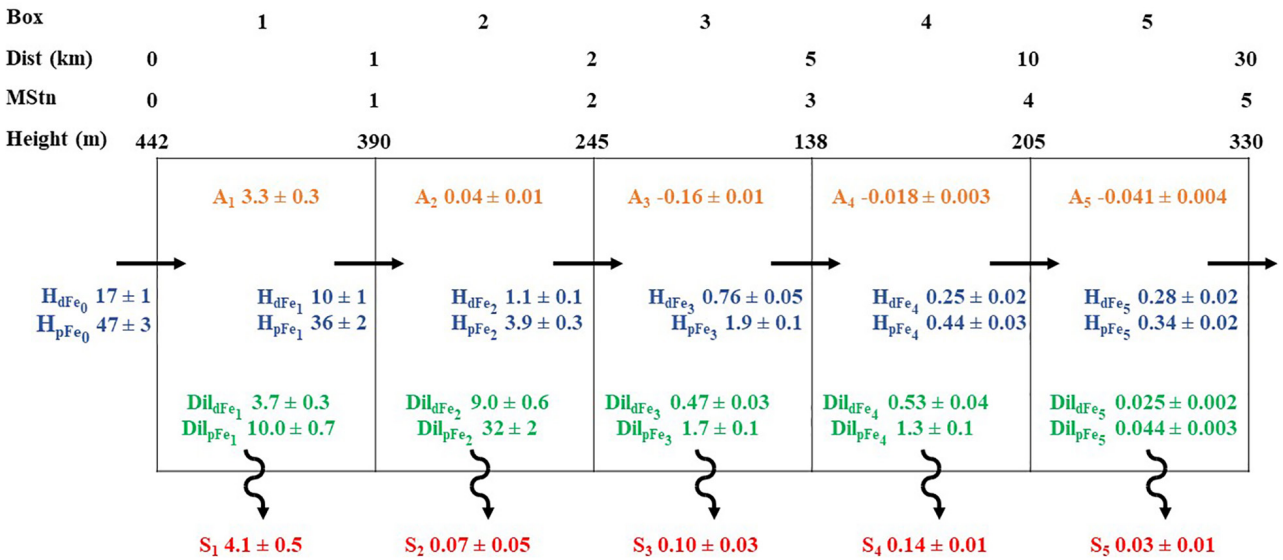

FIGURE 6 | Dissolved and particulate iron 5-box budget of the TAG NBP. Numbers 1–5 on the top correspond to the number of the boxes. Below are depicted the distance from the TAG site, the number of the modeled stations, and the height of the NBP using σ = 27.880 and 27.883 kg m^{-3}. The box-model's $H_{i|n|}$ (in blue), $Dil_{i|n|}$ (in green), $A_{|n|}$ (in orange), and $S_{|n|}$ (in red) are followed by the modeled rate and error from the resolution of model equations combined with a Monte Carlo Method of error propagation. Units are in mol d^{-1}.

TABLE 2 | Box model outputs (horizontal hydrothermal advective fluxes, $H_{i|n|}$ (mol d^{-1}); dispersion and dilution fluxes, $Dil_{i|n|}$ (mol d^{-1}); aggregation/disaggregation fluxes, $A_{|n|}$ (μmol m^{-3} d^{-1}); and sinking fluxes, $S_{|n|}$ (μmol m^{-2} d^{-1}) with errors computed from equations 1–11 using the Monte Carlo method of error propagation.

	0	1 (0–1 km)	2 (1–2 km)	3 (2–5 km)	4 (5–10 km)	5 (10–30 km)
Volume (x10^6 m^3)		**0.416**	**0.318**	**0.668**	**1.620**	**5.350**
H_{dMn} (mol d^{-1})	13.488 ± 0.905	10.606 ± 0.712	1.162 ± 0.078	0.652 ± 0.044	0.201 ± 0.014	0.189 ± 0.013
H_{dFe} (mol d^{-1})	17.120 ± 1.149	10.124 ± 0.680	1.073 ± 0.072	0.761 ± 0.051	0.253 ± 0.017	0.278 ± 0.019
H_{pFe} (mol d^{-1})	46.910 ± 3.149	36.095 ± 2.423	3.915 ± 0.263	1.944 ± 0.131	0.442 ± 0.030	0.344 ± 0.023
H_{TFe} (mol d^{-1})	64.030 ± 4.293	46.219 ± 3.100	4.988 ± 0.334	2.705 ± 0.181	0.694 ± 0.047	0.622 ± 0.042
Dil_{dMn} (mol d^{-1})		2.882 ± 0.211	9.445 ± 0.635	0.509 ± 0.035	0.451 ± 0.030	0.013 ± 0.002
Dil_{dFe} (mol d^{-1})		3.657 ± 0.264	9.015 ± 0.605	0.470 ± 0.032	0.526 ± 0.035	0.016 ± 0.002
Dil_{pFe} (mol d^{-1})		10.022 ± 0.722	32.142 ± 2.158	1.716 ± 0.116	1.344 ± 0.090	0.028 ± 0.004
Dil_{TFe} (mol d^{-1})		13.679 ± 0.984	41.157 ± 2.760	2.186 ± 0.148	1.870 ± 0.126	0.044 ± 0.006
A_{dFe} (μmol m^{-3} d^{-1})		8.025 ± 0.622	0.112 ± 0.036	−0.275 ± 0.022	−0.013 ± 0.002	−0.008 ± 0.001
S_{pFe} (μmol m^{-2} d^{-1})		4130 ± 53	73 ± 46	33 ± 9	17.6 ± 1.6	1.4 ± 0.4

($S_{|n|}$). Both processes produced non-conservative behaviors. We used aggregation and disaggregation in their broad definition. The operationally defined dissolved fraction (<0.45 μm), is the sum of the soluble fraction (<0.02 μm) and the colloidal fraction (between 0.02 and 0.45 μm). In the soluble fraction Fe(II) oxidizes in minutes to Fe(III), which is less soluble (Santana-Casiano et al., 2005). Iron(III) can adsorb to particles in the plume, therefore increasing the Fe content in the measured particulate phase. This would be accounted for in the aggregation process. Conversely, the desorption of Fe from large particles (particulate fraction, >0.45 μm) would be accounted for as a negative aggregation value (disaggregation). In the hydrothermal plume, most of the Fe has been found in the colloidal size fraction (Fitzsimmons et al., 2017; Lough et al., 2019). These nanoparticles can combine, resulting in greater than 0.45 μm particles which would be operationally defined as particulates. As such, the dFe pool depends on the balance between stabilization processes and the reversibility of exchange onto small, sinking particles.

Since the model is assumed to be at steady state, $A_{|n|}$ and $S_{|n|}$ were calculated as follows (Equations 7 and 8).

$$A_{|n|} = H_{dFe|n-1|} - H_{dFe|n|} - Dil_{dFe|n|} \quad (7)$$

$$S_{|n|} = H_{pFe|n-1|} - H_{pFe|n|} - Dil_{pFe|n|} + A_{|n|} \quad (8)$$

Equations 7 and 8 are obtained from the assumption that dMn is a conservative tracer. From this assumption, an excess decrease in dFe that is not proportional to the decrease in dMn is due

to aggregation. Similarly, sinking is the excess loss of pFe with respect to dMn, but it also considers aggregation.

The resulting dMn, dFe, and pFe fluxes estimated in our box model are shown in Equations 9–11.

$$\frac{d(dMn)}{dt}_{|n|} = \frac{1}{v}_{|n|} \cdot (H_{dMn|n-1|} - H_{dMn|n|} - Dil_{dMn|n|}) \quad (9)$$

$$\frac{d(dFe)}{dt}_{|n|} = \frac{1}{v}_{|n|} \cdot (H_{dFe|n-1|} - H_{dFe|n|} - Dil_{dFe|n|} - A_{|n|}) \quad (10)$$

$$\frac{d(pFe)}{dt}_{|n|} = \frac{1}{v}_{|n|} \cdot (H_{pFe|n-1|} - H_{pFe|n|} - Dil_{pFe|n|} - S_{|n|} + A_{|n|}) \quad (11)$$

Model Results and Discussion

The analyzed trace metal data, equations 1–11 were used as the input for a custom MATLAB 9.1 (MathWorks, R2016b) script. To understand the possible uncertainties of our model, we carried out the Monte Carlo method of error propagation. Fluxes and error obtained using the Monte Carlo method, are reported in **Table 2** and displayed in **Figure 6**.

Fate of the Plume Signal

The plume signal rapidly decreased with the increase in distance from the vent site. Dilution and dispersion were responsible for a 21% decrease in the dMn concentration in the first km, which drastically increased to 91% decrease 2 km from the vent site, with $Dil_{dMn|n|}$ rates of 2.9 ± 0.2 and 9.4 ± 0.6 mol d^{-1}, respectively (**Table 2**).

Three plume concentration loss processes, dilution and dispersion, aggregation, and sinking, were identified in our box model as processes affecting the Fe behavior. Where dilution and dispersion caused a concentration loss of dFe and pFe in all boxes; aggregation produced a dFe loss in boxes 1 and 2, and a pFe loss in boxes 3–5; and sinking only affected pFe (**Figure 7**). In the first 30 km, dilution and dispersion of the NBP caused > 99% of the dFe decrease from the NBP, except in the first km from the vent site, where aggregation was responsible for 47% of the dFe decrease. Similarly, dilution and dispersion were the main pFe loss term. Sinking contributed 29% of pFe decrease in the first km, while disaggregation ($A < 0$) combined with sinking caused a 62% pFe decrease in the 10–30 km box.

These NBP loss terms influenced the fate of the plume. When looking at the evolution of its horizontal advection ($H_{dFe|n|}$ and $H_{pFe|n|}$), our results suggest that 93.7 and 91.7% of the hydrothermal dFe and pFe, respectively, had been lost within just 2 km from the vent site. The loss increased to 98.5 and 99.1%, respectively, 10 km from the vent site, and to 98.4 and 99.3% a further 20 km away. These Fe decreases may be due to reversible exchange processes between the dissolved and particulate phases and/or sinking of suspended particles.

Aggregation/Disaggregation Between Dissolved and Particulate Iron

To observe whether reversible exchange dynamics played any role in TAG's NBP dispersal, the dFe/TFe ratio was considered. The dFe/TFe ratio varied through the NBP. At the vent site, aggregation was observed, with the dFe/TFe ratio decreasing from 0.77 at 3580 m to 0.21 at 3255 m (**Figure 5**). Overall, at the vent site inside the NBP, the ratio averaged 0.27. As the NBP dispersed (1 and 2 km away), the dFe/TFe ratio kept decreasing (0.22 and 0.21). At 5, 10, and 30 km away from the vent site, the dFe/TFe ratio increased to 0.28, 0.36, and 0.45, respectively.

This dFe/TFe ratio variability was controlled by changes in the fraction of dFe and/or pFe that was present in the TFe pool. An increase in the ratio may indicate the sinking of pFe (reducing the TFe pool), or the disaggregation of pFe into dFe (maintaining the TFe pool). On the other hand, a decrease in the ratio could also be caused by a decrease in dFe due to aggregation combined with limited sinking. Therefore, dFe/TFe can be used as a first indicator of aggregation or disaggregation processes without any prior information on rates and sources or losses of dFe and pFe.

In the model, the sign of $A_{|n|}$ follows the same pattern as the dFe/TFe ratio,$A_{|n|} > 0$ when the dFe/TFe ratio decreases and vice-versa. This shows that aggregation of dFe predominates in the first km and persists into the second km away from the hydrothermal site, with rates of 8.0 ± 0.6 and 0.11 ± 0.04 nmol L^{-1} d^{-1} respectively. Between 2 and 5 km from the vent site, disaggregation ($A_{|n|} < 0$, −270 ± 20 pmol L^{-1} d^{-1}) becomes more predominant than aggregation. Disaggregation is continuously observed after 5 and 10 km (−13 ± 1 and −8 ± 1 pmol L^{-1} d^{-1}, respectively), although at a much lower rate due to the decrease in the concentration of pFe.

Cheize et al. (2019) calculated the suspended particle dissolution rate during a 14-month period, following the addition of three sediment types collected around Kerguelen Island in the Southern Ocean. During their experiments, they observed net dissolution rates ranging from 1.74 to 7.77 pmol L^{-1} d^{-1}. Even though different minerals were involved in the two different regions, their dissolution rate is in the same order of magnitude as the disaggregation rate calculated in our model between 10 and 30 km from TAG (8 ± 1 pmol L^{-1} d^{-1}), supporting the validity of the hypotheses considered in our model.

Particulate Iron Sinking Fluxes

Particle loss is responsible for the distal metalliferous sediments found below the dispersal trajectories of hydrothermal plumes (Gurvich, 2006). Dividing $S_{|n|}$ by the bottom surface area ($l_{|n|} \cdot w$) of each box, we obtained the average sinking flux in μmol m^{-2} d^{-1} in each box (**Table 2**). The highest pFe sinking flux ($S_{|n|}$) occurred in the first km from the vent site and exponentially decreased as the distance from the vent site increased. High suspended matter was observed in the four stations deployed in the first km (**Figures 2A–D**). The high suspended matter identified an elevated particle load in the seawater, which likely caused the high sinking flux of 4130 ± 530 μmol m^{-2} d^{-1}. In contrast, 10–30 km from the vent site, were the turbidity signal was reaching its limit of detection due to the decrease in particle abundance, the sinking flux decreased three orders of magnitude to 1.4 ± 0.4 μmol m^{-2} d^{-1}. Using dynamic curve fitting, two empirical equations (Equations 12 and 13; μmol m^{-2} d^{-1}) were computed to define the sinking flux by considering the distance at the limits of the boxes and the modeled average sinking rate

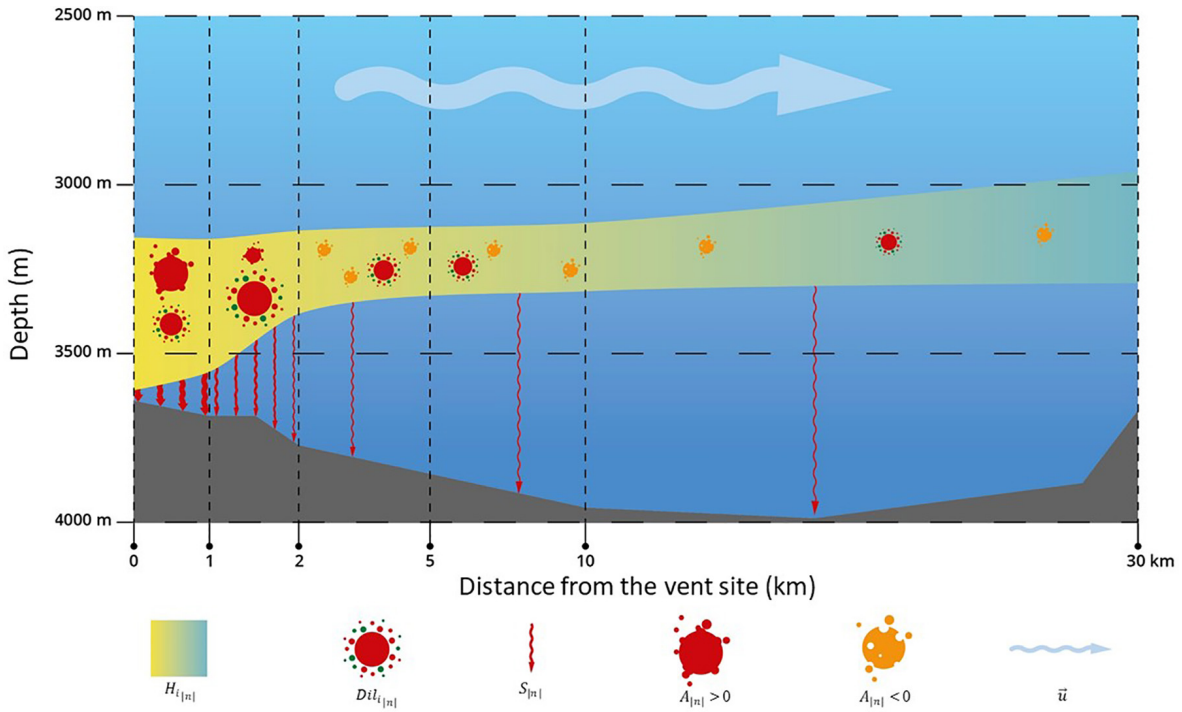

FIGURE 7 | Schematic diagram of the main processes occurring inside the neutrally buoyant plume. The symbol size is representative of the importance of the process with respect to each section of the plume but are not to scale.

within each box. S' considers the sinking rate by using the near boundary of each box ($l_{|0|}$ to $l_{|n-1|}$), therefore producing the fastest sinking rate; while S'' considers the sinking rate using the far boundary of each box ($l_{|1|}$ to $l_{|n|}$), with the corresponding slower sinking rate. These two equations create an envelope were the theoretical sinking rate at a distance (dist; in m) from the vent site could stand between S' and S''.

$$S' = 38 + 4093 \times e^{-4.7 \times dist} - 3.8 \times dist \tag{12}$$

$$S'' = 34 + 400000 \times e^{-4.6 \times dist} - 1.1 \times dist \tag{13}$$

Equations 12 and 13 were tested against the available Fe fluxes obtained from sediment trap measurements situated below a NBP. Toner et al. (2009) presented particle mass flux and total Fe weight% collected in sediment traps deployed ∼5 m above the sea floor (∼2,500 m depth) and ∼100 m west of the Tica vent on the East Pacific Rise, a vent situated in a fast spreading ridge in the Pacific Ocean. Using their maximum particle flux (29.9 mg m^{-2} d^{-1}) and average total Fe weight% (2.69%) we obtained a flux of 14.4 μmol m^{-2} d^{-1}. This flux is in the same range of variation as our estimated sinking flux, which provides some certainty in the order of magnitude of our results and further highlights the importance of studying the Fe-rich particle loss from the NBP which might affect other particle-reactive TEIs (German et al., 2016). Using Equations 12 and 13, the observed flux would be achieved in a sediment trap just below the NBP at a distance between 6.2 and 17.8 km from the vent site. For this sediment trap situated in a fast spreading ridge, Equations 12 and 13 underestimate the sinking flux, likely due to the difference in geology and chemistry between the vents from two contrasting spreading ridges, the vertical separation between the NBP and the sediment trap, and the faster dissipation of TAG's hydrothermal plume.

Size and Sinking Velocity of pFe Loss

The sinking velocity of pFe could be estimated using Equation 14.

$$v_{|n|} = \frac{S_{|n|}}{[I_{|n|}] \cdot l_{|n|} \cdot w} \tag{14}$$

Values were equal to 45 ± 6 m d^{-1} in the first km and decreased to 5 ± 2 m d^{-1} between 1 and 10 km from TAG. Our settling velocity were in the same order of magnitude as those obtained by German and Sparks (1993), who estimated settling velocities (v) from 4 to 8 m d^{-1} for coarse particles (5 μm radius) and from 0.2 to 0.3 m d^{-1} for fine-grained particles (1 μ m radius).

Using Stokes' Law (Equation 15) and our $v_{|n|}$ values, we could estimate particle sizes.

$$v = \frac{2 \cdot g \cdot r^2 \Delta\rho}{9 \cdot \mu_w} \tag{15}$$

Where g = gravitational acceleration (9.81 m s^{-2}); r = particle radius (m); $\Delta\rho$ = the density difference between the particle and the fluid; and μ = the dynamic viscosity of water (kg m^{-1} s^{-1}).

μ_w was obtained from Sharqawy et al. (2010) equations (Equations 16–19)

$$\mu_{SW} = \mu_W \cdot \left(1 + A \cdot \frac{sal}{1000} + B \cdot \left(\frac{sal}{1000}\right)^2\right) \quad (16)$$

$$\mu_W = 4.2844 \times 10^{-5} + (0.157 \cdot (t + 64.993)^2 - 91.296)^{-1} \quad (17)$$

$$A = 1.541 + 1.998 \times 10^{-2} \cdot t - 9.52 \times 10^{-5} \cdot t^2 \quad (18)$$

$$B = 7.974 - 7.561 \times 10^{-2} \cdot t + 4.724 \times 10^{-4} \cdot t^2 \quad (19)$$

Where sal, Salinity; t, temperature (°C).

To evaluate $\Delta\rho$, we used the same range of particle densities (2400 – 3600 kg m^{-3} for goethite and amorphous Fe oxyhydroxides) as German and Sparks (1993), who calculated particles ranging between 1 and 10 μm. The resulting modeled particle radii ranged between 14 and 20 μm in the first km from TAG and decreased to 2–4 μm between 2 and 30 km from TAG. Our particle size ranges also agree at distances greater than 1 km with aggregates observed by SEM-EDS imaging on filters collected during our cruise (unpublished data).

Particle Re-entrainment

Another fate of particulate material from hydrothermal plumes is re-entrainment and recycling, by which precipitating particles are re-incorporated into the BP. Re-entrainment is proportional to the volume flow rate of the plume (volumetric flow rate into the base of the radially spreading plume) (German and Sparks, 1993). Due to TAG's volume flow rate, re-entrainment affects the particulate matter transport. Re-entrainment of suspended particulate matter from the TAG hydrothermal plume has been calculated previously as ranging from 31 to 77% (Rudnicki and Elderfield, 1992) and from 43 to 89% (Speer and Rona, 1989) which led to the conclusion that more than 50% of the suspended particulate matter at the TAG hydrothermal plume was being re-entrained (German and Sparks, 1993). Based on this conclusion, and assuming that 50% of $S_{|1|}$ was re-entrained into $H_{pFe|1|}$, ∼5% of the pFe influx in the vent site station does not come directly from the hydrothermal vent, but has been re-entrained. This means that re-entrainment could be a significant source of particulate material in NBP dispersion models. This can of course have profound effects on both the concentrations and residence times of elements within the plume.

CONCLUSION

The HERMINE cruise was a GEOTRACES process study (GApr07), which focused on the 75 km range horizontal transport of the TAG hydrothermal plume. This allowed for the positioning of 4 profile stations 1 km or closer to the vent site. At these four stations, θ, *S*, nephelometry and TM concentrations varied within the plume. A possible explanation is that these observations result from having a multi-phase plume which separated them due to the horizontal current.

During the first 10 km of the NBP transport, it ascended 45 m and its vertical spread decreased to 205 m (a 54% reduction), following local water masses, as identified by σ. This behavior shows that water mass characterization should be taken into account when modeling the dispersion of the NBP. Furthermore, the dominance of the dilution and diffusion flux determined using dMn as a conservative tracer in a steady-state box model (see Section "Fate of the plume signal"), showed the importance of transport in the NBP transverse axis, therefore, future work considering not only the vertical axis but the transverse axis in NBP should be undertaken, giving a spatial view on the variation of the width of the NBP.

Our box model, schematically summarized in **Figure 7**, was able to define the distance range where the main reversible exchange direction between the dissolved and the particulate phases starts taking place, somewhere between 1 and 5 km from the vent site (see section "Size and sinking velocity of pFe loss"). Aggregation predominates in the first 2 km while disaggregation outweighs aggregation further away. Our model results also suggest that the Fe loss by sinking was due to particles with radii ranging from 1.9 to 19.6 μm, with decreasing sizes as the NBP was transported away from the vent site. Even though there was a fast decrease in the particulate content in the first 2 km, and the loss rate followed an exponential decrease equation (Equations 12 and 13) as observed in other hydrothermal systems (Field and Sherrell, 2000; Fitzsimmons et al., 2017), the hydrothermal dFe and dMn signal could still be seen 75 km from the TAG vent site.

Limited work has been carried out in slow-spreading ridges compared to fast-spreading ridges, consequently, the lack of data makes it difficult to constrain models for these regions (German et al., 2015). The approach presented here could allow better modeling of hydrothermal sources and the computed equations should be tested in other sites situated in the MAR, such as the ultramafic-hosted hydrothermal Rainbow site (36° 15′N) (German et al., 1996) to elucidate the aggregation and particle dispersion processes at play in a different geodynamic context. This northward site has particle enrichment similar to TAG, where nephelometry shows hydrothermal anomalies extending 10 – 15 km, comparable to our suspended matter anomaly (10 – 30 km). Therefore, the coupling of the model described in this study with ocean circulation models could further define the NBP dispersion from similar vent sites, improving hydrothermal modeling and constraining the station spacing in future research depending on the research goals. Furthermore, we provide the required data for future modeling studies on the relatively unknown contribution of slow-spreading ridges, with respect to fast-spreading ridges, as sources of trace metals (German et al., 2016).

DATA AVAILABILITY STATEMENT

All datasets generated for this study are included in the article/**Supplementary Material**.

AUTHOR CONTRIBUTIONS

YF, EP, and CC acquired the funding for the cruise and supervised the research cruise. HP and MC were in charge of the trace metal sampling while HW, AG, and TH collected the samples at sea. DG-S and HP analyzed the dTM samples while HP and MC analyzed the pTM samples. DG-S, GS, HP, and MC developed the box-model. DG-S wrote the manuscript with significant contributions from all co-authors. All the authors contributed to the article and approved the submitted version.

FUNDING

This work was supported by the French National Research Agency (12-PDOC-0025-01) to HP and by the LabexMER (ANR-10-LABX-19) to HP ("GEOTAG") and CC ("TRANSE-METH"), and by the Ifremer. For the logistics, it was supported by DT-INSU and GENAVIR. This work was funded by the Graduate School of the Université de Bretagne Occidentale (DGS), and the IFREMER REMIMA project. This work was also supported by the "Laboratoire d'Excellence" LabexMER (ANR-10-LABX-19) and co-funded by a grant from the French Government under the program "Investissements d'Avenir" (TRANS-METH project). The data has been submitted to the GEOTRACES International Data Assembly Centre (https://www.bodc.ac.uk/geotraces/data).

ACKNOWLEDGMENTS

The authors would like to thank the captain and crew of the N/O *Pourquoi pas*? as well as the scientific team during the HERMINE cruise. Special thanks to Mickael Roudaut for managing the rosette sniffing for the NBP.

SUPPLEMENTARY MATERIAL

The Supplementary Material for this article can be found online at: https://www.frontiersin.org/articles/10.3389/fmars.2020.00568/full#supplementary-material

REFERENCES

Bennett, S. A., Achterberg, E. P., Connelly, D. P., Statham, P. J., Fones, G. R., and German, C. R. (2008). The distribution and stabilisation of dissolved Fe in deep-sea hydrothermal plumes. *Earth Planet. Sci. Lett.* 270, 157–167. doi: 10.1016/j.epsl.2008.01.048

Boyd, P. W., and Ellwood, M. J. (2010). The biogeochemical cycle of iron in the ocean. *Nat. Geosci.* 3, 675–682. doi: 10.1038/ngeo964

Cheize, M., Planquette, H., Fitzsimmons, J. N., Pelleter, E., Sherrell, R. M., Lambert, C., et al. (2019). Contribution of resuspended sedimentary particles to dissolved iron and manganese in the ocean: an experimental study. *Chem. Geol.* 511, 389–415. doi: 10.1016/j.chemgeo.2018.10.003

Cheize, M., Planquette, H., González-Santana, D., Whitby, H., Gourain, A., Holmes, T., et al. (2018). "High resolution particulate trace metals dispersion from the tag hydrothermal vent (Mid-Atlantic Ridge)," in *Goldschmidt Conference* (Boston, MA), 376.

Chiba, H., Masuda, H., Lee, S. Y., and Fujioka, K. (2001). Chemistry of hydrothermal fluids at the TAG active mound, MAR 26, in 1998. *Geophys. Res. Lett.* 28, 2919–2922. doi: 10.1029/2000GL012645

Conway, T. J., and John, S. G. (2014). Quantification of dissolved iron sources to the North Atlantic Ocean. *Nature* 511, 212–215. doi: 10.1038/nature13482

Edmonds, H. N., German, C. R., Green, D. R. H., Huh, Y., Gamo, T., and Edmond, J. M. (1996). Continuation of the hydrothermal fluid chemistry time series at TAG, and the effects of ODP drilling. *Geophys. Res. Lett.* 23, 3487–3489. doi: 10.1029/96GL01597

Elderfield, H. (1977). Chapter 9 the form of manganese and iron in marine sediments. *Elsevier Oceanogr. Ser.* 15, 269–289. doi: 10.1016/S0422-9894(08)71023-7

Field, M. P., and Sherrell, R. M. (2000). Dissolved and particulate Fe in a hydrothermal plume at 9°45′N, East Pacific Rise: slow Fe (II) oxidation kinetics in Pacific plumes. *Geochim. Cosmochim. Acta* 64, 619–628. doi: 10.1016/S0016-7037(99)00333-6

Fitzsimmons, J. N., Carrasco, G. G., Wu, J., Roshan, S., Hatta, M., Conway, T. J., et al. (2015). Partitioning of dissolved iron and iron isotopes into soluble and colloidal phases along the GA03 GEOTRACES North Atlantic Transect. *Deep Sea Res. Part II Top. Stud. Oceanogr.* 116, 130–151.

Fitzsimmons, J. N., John, S. G., Marsay, C. M., Hoffman, C. L., Nicholas, S. L., Toner, B. M., et al. (2017). Iron persistence in a distal hydrothermal plume supported by dissolved-particulate exchange. *Nat. Geosci.* 10, 195–201. doi: 10.1038/ngeo2900

German, C. R., Campbell, A. C., and Edmond, J. M. (1991a). Hydrothermal scavenging at the mid-atlantic ridge: modification of trace element dissolved fluxes. *Earth Planet. Sci. Lett.* 107, 101–114. doi: 10.1016/0012-821X(91)90047-L

German, C. R., Fleer, A. P., Bacon, M. P., and Edmond, J. M. (1991b). Hydrothermal scavenging at the mid-atlantic ridge: radionuclide distributions. *Earth Planet. Sci. Lett.* 105, 170–181. doi: 10.1016/0012-821X(91)90128-5

German, C. R., Klinkhammer, G. P., and Rudnicki, M. D. (1996). The Rainbow hydrothermal plume, 36°15′N. *MAR. Geophys. Res. Lett.* 23, 2979–2982. doi: 10.1029/96GL02883

German, C. R., Legendre, L. L., Sander, S. G., Niquil, N., Luther, G. W., Bharati, L., et al. (2015). Hydrothermal Fe cycling and deep ocean organic carbon scavenging: model-based evidence for significant POC supply to seafloor sediments. *Earth Planet. Sci. Lett.* 419, 143–153. doi: 10.1016/j.epsl.2015.03.012

German, C. R., and Sparks, R. S. J. (1993). Particle recycling in the TAG hydrothermal plume. *Earth Planet. Sci. Lett.* 116, 129–134. doi: 10.1016/0012-821X(93)90049-F

German, C. R., Casciotti, K. A., Dutay, J.-C., Heimbürger, L. E., Jenkins, W. J., Measures, C. I., et al. (2016). Hydrothermal impacts on trace element and isotope ocean biogeochemistry. *Philos. Trans. R. Soc. A Math. Phys. Eng. Sci.* 374:20160035. doi: 10.1098/rsta.2016.0035

Goto, S., Gamo, T., Chiba, H., Fujioka, K., and Mitsuzawa, K. (2007). Contribution of heat outputs from high- and low-temperature hydrothermal sources to the neutrally buoyant plume at the TAG hydrothermal mound. *Mid-Atlantic Ridge. Earth, Planets Sp.* 59, 1141–1146. doi: 10.1186/BF03352057

Gurvich, E. G. (ed.) (2006). "Recent metalliferous sediments in the oceans BT," in *Metalliferous Sediments of the World Ocean: Fundamental Theory of Deep-Sea Hydrothermal Sedimentation*, (Berlin: Springer), 7–126.

Hatta, M., Measures, C. I., Wu, J., Roshan, S., Fitzsimmons, J. N., Sedwick, P. N., et al. (2015). An overview of dissolved Fe and Mn distributions during the 2010–2011 U.S. GEOTRACES north Atlantic cruises: GEOTRACES GA03. *Deep Sea Res. Part II Top. Stud. Oceanogr.* 116, 117–129. doi: 10.1016/j.dsr2.2014.07.005

Johnson, K. S., Michael Gordon, R., and Coale, K. H. (1997). What controls dissolved iron concentrations in the world ocean? *Mar. Chem.* 57, 137–161. doi: 10.1016/S0304-4203(97)00043-1

Klinkhammer, G. P., Elderfield, H., Greaves, M., Rona, P. A., and Nelsen, T. A. (1986). Manganese geochemistry near high-temperature vents in the Mid-Atlantic Ridge rift valley. *Earth Planet. Sci. Lett.* 80, 230–240. doi: 10.1016/0012-821X(86)90107-X

Lagerström, M. E., Field, M. P., Séguret, M., Fischer, L., Hann, S., and Sherrell, R. M. (2013). Automated on-line flow-injection ICP-MS determination of trace metals (Mn, Fe, Co, Ni, Cu and Zn) in open ocean seawater: application to the GEOTRACES program. *Mar. Chem.* 155, 71–80. doi: 10.1016/j.marchem.2013.06.001

Lalou, C., Reyss, J., Brichet, E., Rona, P. A., and Thompson, G. (1995). Hydrothermal activity on a 10ˆ5-year scale at a slow-spreading ridge, TAG hydrothermal field, Mid-Atlantic Ridge 26° N. *J. Geophys. Res. Solid Earth* 100, 17855–17862. doi: 10.1029/95JB01858

Lough, A. J. M., Homoky, W. B., Connelly, D. P., Comer-Warner, S. A., Nakamura, K., Abyaneh, M. K., et al. (2019). Soluble iron conservation and colloidal iron dynamics in a hydrothermal plume. *Chem. Geol.* 511, 225–237. doi: 10.1016/j.chemgeo.2019.01.001

Luther, G. W., Kostka, J. E., Church, T. M., Sulzberger, B., and Stumm, W. (1992). Seasonal iron cycling in the salt-marsh sedimentary environment: the importance of ligand complexes with Fe (II) and Fe (III) in the dissolution of Fe (III) minerals and pyrite, respectively. *Mar. Chem.* 40, 81–103.

Machado-Infante, J., Ramírez-Caballero, G., and Barajas-Meneses, M. (2016). Study of the adsorption capacity of Fe(II) dissolved in water by using a mineral rich in Manganese Dioxide (MnO2) from Colombia. *DYNA* 83, 223–228.

Martin, J. H., and Fitzwater, S. E. (1988). Iron deficiency limits phytoplankton growth in the north-east Pacific subarctic. *Nature* 331, 341–343. doi: 10.1038/331341a0

Mastin, M. (2020). *Étude Tridimensionnelle du Panache Hydrothermal du site TAG : Identification des Processus D'export et de Vieillissement du Panache. Master Sciences de la Mer et du Littoral, Chimie de l'Environnement Marin, M2 Report. UBO. Supervisor: Cécile Cathalot.*

Measures, C., Hatta, M., Fitzsimmons, J., and Morton, P. (2015). Dissolved Al in the zonal N Atlantic section of the US GEOTRACES 2010/2011 cruises and the importance of hydrothermal inputs. *Deep Sea Res. Part II Top. Stud. Oceanogr.* 116, 176–186.

Middag, R., De Baar, H. J. W., Laan, P., and Bakker, K. (2009). Dissolved aluminium and the silicon cycle in the Arctic Ocean. *Mar. Chem.* 115, 176–195.

Middag, R., Van Slooten, C., De Baar, H. J. W., and Laan, P. (2011). Dissolved aluminium in the Southern Ocean. *Deep Sea Res. Part II Top. Stud. Oceanogr.* 58, 2647–2660.

Millero, F. J., Sotolongo, S., and Izaguirre, M. (1987). The oxidation kinetics of Fe(II) in seawater. *Geochim. Cosmochim. Acta* 51, 793–801. doi: 10.1016/0016-7037(87)90093-7

Mills, R. A., Wells, D. M., and Roberts, S. (2001). Genesis of ferromanganese crusts from the TAG hydrothermal field. *Chem. Geol.* 176, 283–293. doi: 10.1016/S0009-2541(00)00404-6

Nelsen, T. A., Klinkhammer, G. P., Trefry, J. H., and Trocine, R. P. (1987). Real-time observation of dispersed hydrothermal plumes using nephelometry: examples from the Mid-Atlantic Ridge. *Earth Planet. Sci. Lett.* 81, 245–252. doi: 10.1016/0012-821X(87)90160-9

Nishioka, J., Obata, H., and Tsumune, D. (2013). Evidence of an extensive spread of hydrothermal dissolved iron in the Indian Ocean. *Earth Planet. Sci. Lett.* 361, 26–33.

Noble, A. E., Lamborg, C. H., Ohnemus, D. C., Lam, P. J., Goepfert, T. J., Measures, C. I., et al. (2012). Basin-scale inputs of cobalt, iron, and manganese from the Benguela-Angola front to the South Atlantic Ocean. *Limnol. Oceanogr.* 57, 989–1010.

Pichler, T., and Veizer, J. (1999). Precipitation of Fe(III) oxyhydroxide deposits from shallow-water hydrothermal fluids in Tutum Bay, Ambitle Island, Papua New Guinea. *Chem. Geol.* 162, 15–31. doi: 10.1016/S0009-2541(99)00068-6

Planquette, H., and Sherrell, R. M. (2012). Sampling for particulate trace element determination using water sampling bottles: methodology and comparison to in situ pumps. *Limnol. Oceanogr. Methods* 10, 367–388. doi: 10.4319/lom.2012.10.367

Resing, J. A., Sedwick, P. N., German, C. R., Jenkins, W. J., Moffett, J. W., Sohst, B. M., et al. (2015). Basin-scale transport of hydrothermal dissolved metals across the South Pacific Ocean. *Nature* 523, 200–203. doi: 10.1038/nature14577

Rona, P. A. (1980). TAG hydrothermal field: mid-atlantic ridge crest at latitude 26°N. *J. Geol. Soc. London.* 137, 385–402. doi: 10.1144/gsjgs.137.4.0385

Rona, P. A. (2005). "TAG hydrothermal field: a key to modern and ancient seafloor hydrothermal VMS ore-forming systems BT," in *Mineral Deposit Research: Meeting the Global Challenge*, eds J. Mao and F. P. Bierlein (Berlin: Springer), 687–690.

Rona, P. A., Klinkhammer, G. P., Nelsen, T. A., Trefry, J. H., and Elderfield, H. (1986). Black smokers, massive sulphides and vent biota at the Mid-Atlantic Ridge. *Nature* 321, 33–37. doi: 10.1038/321033a0

Rona, P. A., and Speer, K. G. (1989). An atlantic hydrothermal plume: trans-atlantic geotraverse (TAG) area, Mid-Atlantic Ridge crest near 26°N. *J. Geophys. Res. Solid Earth* 94, 13879–13893. doi: 10.1029/JB094iB10p13879

Rudnicki, M. D., and Elderfield, H. (1992). Theory applied to the Mid-Atlantic ridge hydrothermal plumes: the finite-difference approach. *J. Volcanol. Geotherm. Res.* 50, 161–172. doi: 10.1016/0377-0273(92)90043-D

Rudnicki, M. D., and Elderfield, H. (1993). A chemical model of the buoyant and neutrally buoyant plume above the TAG vent field, 26 degrees N. Mid-Atlantic Ridge. *Geochim. Cosmochim. Acta* 57, 2939–2957. doi: 10.1016/0016-7037(93)90285-5

Saito, M. A., Noble, A. E., Tagliabue, A., Goepfert, T. J., Lamborg, C. H., and Jenkins, W. J. (2013). Slow-spreading submarine ridges in the South Atlantic as a significant oceanic iron source. *Nat. Geosci.* 6, 775–779. doi: 10.1038/ngeo1893

Sander, S. G., and Koschinsky, A. (2011). Metal flux from hydrothermal vents increased by organic complexation. *Nat. Geosci.* 4, 145–150. doi: 10.1038/ngeo1088

Santana-Casiano, J. M., González-Dávila, M., and Millero, F. J. (2005). Oxidation of nanomolar level of Fe(II) with oxygen in natural waters. *Environ. Sci. Technol.* 39, 2073–2079. doi: 10.1021/es049748y

Sharqawy, M. H., Lienhard, V. J. H., and Zubair, S. M. (2010). The thermophysical properties of seawater: a review of existing correlations and data. *Desalin. Water Treat.* 16, 354–380. doi: 10.5004/dwt.2010.1079

Socolofsky, S., and Adams, E. (2002). Multi-phase plumes in uniform and stratified crossflow. *J. Hydraul. Res.* 40, 661–672. doi: 10.1080/00221680209499913

Speer, K. G., and Marshall, J. (1995). The growth of convective plumes at seafloor hot springs. *J. Mar. Res.* 53, 1025–1057. doi: 10.1357/0022240953212972

Speer, K. G., and Rona, P. A. (1989). A model of an Atlantic and Pacific hydrothermal plume. *J. Geophys. Res.* 94, 6213–6220. doi: 10.1029/jc094ic05p06213

Statham, P. J., German, C. R., and Connelly, D. P. (2005). Iron (II) distribution and oxidation kinetics in hydrothermal plumes at the Kairei and Edmond vent sites, Indian Ocean. *Earth Planet. Sci. Lett.* 236, 588–596. doi: 10.1016/J.EPSL.2005.03.008

Statham, P. J., Yeats, P. A., and Landing, W. M. (1998). Manganese in the eastern Atlantic Ocean: processes influencing deep and surface water distributions. *Mar. Chem.* 61, 55–68.

Tagliabue, A., Bopp, L., Dutay, J. C., Bowie, A. R., Chever, F., Jean-Baptiste, P., et al. (2010). Hydrothermal contribution to the oceanic dissolved iron inventory. *Nat. Geosci.* 3, 252–256. doi: 10.1038/ngeo818

Tagliabue, A., Bowie, A. R., Boyd, P. W., Buck, K. N., Johnson, K. S., and Saito, M. A. (2017). The integral role of iron in ocean biogeochemistry. *Nature* 543, 51–59. doi: 10.1038/nature21058

Tagliabue, A., and Resing, J. A. (2016). Impact of hydrothermalism on the ocean iron cycle. *Philos. Trans. R. Soc. A Math. Phys. Eng. Sci.* 374:20150291. doi: 10.1098/rsta.2015.0291

Toner, B. M., Fakra, S. C., Manganini, S. J., Santelli, C. M., Marcus, M. A., Moffett, J. W., et al. (2009). Preservation of iron(II) by carbon-rich matrices in a hydrothermal plume. *Nat. Geosci.* 2, 197–201. doi: 10.1038/ngeo433

van Haren, H., Duineveld, G., and de Stigter, H. (2017). Prefrontal bore mixing. *Geophys. Res. Lett.* 44, 9408–9415.

van Hulten, M., Middag, R., Dutay, J.-C., de Baar, H., Roy-Barman, M., Gehlen, M., et al. (2017). Manganese in the west Atlantic Ocean in the context of the first

global ocean circulation model of manganese. *Biogeosciences* 14, 1123–1152. doi: 10.5194/bg-14-1123-2017

Von Damm, K. L. (1995). Controls on the chemistry and temporal variability of seafloor hydrothermal fluids. *Seafloor hydrothermal Syst. Phys. Chem. Biol. Geol. Interact.* 91, 222–247. doi: 10.1029/GM091p0222

Wichers, S. (2005). *Verification of Numerical Models for Hydrothermal Plume Water Through Field Measurements at TAG*. Master Thesis, MIT-WHOI, Cambridge, MA.

Yücel, M., Gartman, A., Chan, C. S., and Luther, G. W. (2011). Hydrothermal vents as a kinetically stable source of iron-sulphide-bearing nanoparticles to the ocean. *Nat. Geosci.* 4, 367–371.

Conflict of Interest: The authors declare that the research was conducted in the absence of any commercial or financial relationships that could be construed as a potential conflict of interest.